

Contents lists available at ScienceDirect

# Nanomedicine: Nanotechnology, Biology, and Medicine

journal homepage: www.sciencedirect.com/journal/nanomedicine-nanotechnologybiology-and-medicine



# Original Article



Membrane cholesterol enrichment and folic acid functionalization lead to increased accumulation of erythrocyte-derived optical nano-constructs within the ovarian intraperitoneal tumor implants in mice

Chi-Hua Lee, PhD <sup>a</sup>, Jenny Mac, PhD <sup>a</sup>, Taylor Hanley, PhD <sup>b</sup>, Shamima Zaman, MS <sup>b</sup>, Raviraj Vankayala, PhD <sup>b,1</sup>, Bahman Anvari, PhD <sup>a,b,\*</sup>

#### ARTICLE INFO

# Keywords: Biomimetics Drug delivery Nanomaterials Near infrared fluorescence imaging Red blood cells

## ABSTRACT

Cytoreductive surgery remains as the gold standard to treat ovarian cancer, but with limited efficacy since not all tumors can be intraoperatively visualized for resection. We have engineered erythrocyte-derived nano-constructs that encapsulate the near infrared (NIR) fluorophore, indocyanine green (ICG), as optical probes for NIR fluorescence imaging of ovarian tumors. Herein, we have enriched the membrane of these nano-constructs with cholesterol, and functionalized their surface with folic acid (FA) to target the folate receptor- $\alpha$ . Using a mouse model, we show that the average fraction of the injected dose per tumor mass for nano-constructs with both membrane cholesterol enrichment and FA functionalization was  $\sim$  sixfold higher than non-encapsulated ICG,  $\sim$  twofold higher than nano-constructs enriched with cholesterol alone, and 33 % higher than nano-constructs with only FA functionalization at 24-h post-injection. These results suggest that erythrocyte-derived nano-constructs containing both cholesterol and FA present a platform for improved fluorescence imaging of ovarian tumors.

## Introduction

Ovarian cancer is the deadliest gynecological cancer in women with estimated 20,000 new cases and 13,000 deaths in 2023. The majority of women with ovarian cancer are diagnosed at the late stage when the tumor has spread beyond the ovaries and become a peritoneal disease. Cytoreductive surgery (CS) followed by chemotherapy remains as the gold standard method of treatment. One of the most important prognostic factors is the degree of CS, with improved survival associated with complete resection of all visible cancer. A challenge during CS is the lack of the ability by the surgeon to visualize small tumor nodules (< 1 mm) for resection, leading to incomplete removal of tumors and ultimately recurrence. Therefore, there is a clinical need for the development of intraoperative imaging capabilities to provide visual guidance for resection of all tumors.

Near infrared (NIR) wavelengths ( $\sim 700\text{--}2500~\text{nm})$  for fluorescence imaging are particularly advantageous since there is minimal tissue autofluorescence over the NIR spectral band. When combined with administration of exogenous fluorescent materials, imaging contrast is

improved.<sup>4</sup> Indocyanine green (ICG) is an FDA-approved NIR dye for specific clinical usage such as ophthalmological angiography.<sup>5,6</sup> ICG has also been utilized clinically to investigate its efficacy for NIR intra-operative fluorescence imaging of metastatic ovarian tumors.<sup>7</sup> Despite the demonstrated feasibility to image malignant lesions, results of this study showed a high false positive rate of 62 %. Upon a bolus intra-vascular injection, ICG clears from the vasculature in a biexponential manner with a half-life of the initial phase on the order of about 10 min or less.<sup>8–10</sup> Previous studies indicate that ICG rapidly binds to albumin and high density lipo-proteins, and is cleared from circulation primary by the liver, and eliminated through the hepatobiliary mechanism.<sup>11</sup>, <sup>12</sup> Therefore, there is a need for methodologies that would result in greater bioavailability and specificity of ICG for tumor targeting.

Encapsulation of ICG into nano-sized particles provides a method to shield ICG from non-specific interactions with plasma proteins and extend its circulation time. Additionally, use of nano-sized particles allows for the delivery of encapsulated cargo to the tumors due to the enhanced permeability and retention (EPR) effect. <sup>13,14</sup> Nano-sized platforms fabricated from red blood cells (RBCs) (erythrocytes) have

<sup>&</sup>lt;sup>a</sup> Department of Biochemistry, University of California, Riverside, 900 University Avenue, Riverside, CA 92521, USA

b Department of Bioengineering, University of California, Riverside, 900 University Avenue, Riverside, CA 92521, USA

<sup>\*</sup> Corresponding author at: Department of Bioengineering, University of California, Riverside, 900 University Avenue, Riverside, CA 92521, USA. *E-mail address:* anvarib@ucr.edu (B. Anvari).

<sup>1</sup> Present address for Author R.V.: Department of Bioscience and Bioengineering, Indian Institute of Technology, Jodhpur, Rajasthan 342,037 India.

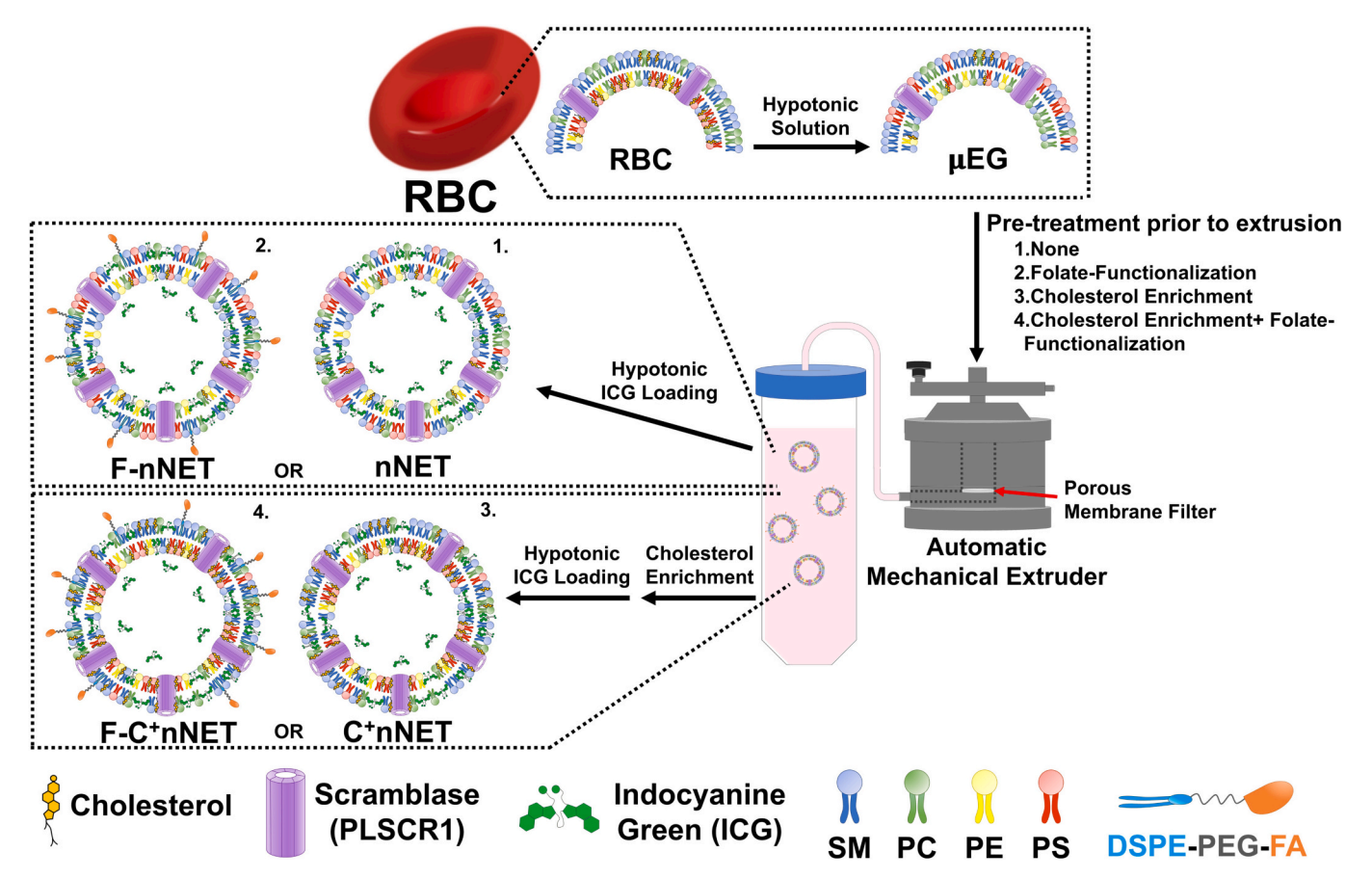


Fig. 1. Schematic of the methodology to fabricate nNETs variants. First, RBCs were treated with hypotonic PBS to deplete the hemoglobin and form micro-sized erythrocyte ghosts (μEGs). To form variants of nNETs variants, prior to extrusion, μEGs were subject to: (1) no treatment followed by extrusion to nano-scale (< 200 nm) and hypotonic loading of ICG loading to form nNETs; (2) functionalization with DSPE-PEG-FA followed by extrusion and ICG loading to form F-nNETs; (3) enrichment of membrane with cholesterol, followed by extrusion, repeated cholesterol enrichment, and loading of ICG to form C<sup>+</sup>nNETs; and (4) simultaneous functionalization with DSPE-PEG-FA and membrane cholesterol enrichment, followed by extrusion, repeated cholesterol enrichment, and ICG loading to form F-C<sup>+</sup>nNETs. SM: Sphingomyelin, PC: Phosphatidylcholine, PE: Phosphatidylethanolamine, PS: Phosphatidylserine.

emerged as carriers for delivery of various therapeutic or imaging cargos, including ICG.  $^{15-19}$  We refer to constructs fabricated from RBCs and loaded with ICG as near infrared erythrocyte-derived transducers (NETs). A particular feature of RBC-based platforms is their naturally long circulation time ( $\sim 90{\text -}120$  days), attributed to the presence specific membrane proteins including CD47 which signals with phagocyte receptor SIRP $\alpha$  to evade elimination by macrophages,  $^{20,21}$  CD55 which protects against cell lysis by the complement system, and CD59 which blocks the assembly of membrane-attack complexes.  $^{20,22}$  Our proteomic results indicate that these membrane proteins are retained in ICG-loaded nanoparticles fabricated from RBCs.  $^{23}$ 

Common methods to encapsulate various cargos into RBC-based nano-constructs are based on hypotonic treatment and extrusion of the red blood cells (RBCs). However, such methods can cause flipping of phosphatidylserine (PS), one of the major membrane phospholipids, from the inner leaflet where it is normally located in the RBCs, <sup>24</sup> to the outer leaflet. <sup>25</sup> Flipping of PS to the outer leaflet serves as a recognition signal for phagocytic removal by splenic macrophages. <sup>26–28</sup> As such, RBC-based carriers with surface-exposed PS are susceptible to clearance by macrophages, resulting in lower quantities to reach a desired site of interest such as a tumor.

Previously, we reported that membrane cholesterol enrichment of micro-sized NETs ( $\mu$ NETs) provides an effective method to reduce PS flipping to the outer leaflet, resulting in prolonged bloodstream circulation in healthy Swiss Webster mice. <sup>29</sup> One aspect of the present study is to evaluate if enriching the membrane of nano-sized NETs (nNETs) with cholesterol would result in higher quantities in bloodstream and

intraperitoneal ovarian tumor implants in immunodeficient mice post tail-vein injection as compared nNETs without membrane cholesterol enrichment. Another aspect of the study relates to surface functionalization of nNETs with folic acid (FA) to target the Folate receptor- $\alpha$ , which is overexpressed on the tumors in majority of patients with ovarian cancers, both in primary tumor tissue and metastatic tumor deposits. <sup>30,31</sup> Herein, we also evaluate the effects of FA functionalization in addition to membrane cholesterol enrichment on the biodistribution of these nanoparticles in various organs and intraperitoneal ovarian tumor implants, and compare the results to the nano-constructs functionalized with FA or enriched with cholesterol alone.

## Materials and methods

## Fabrication of nano-constructs

A schematic of the process for fabrication of nNETs variants is presented in Fig. 1. RBCs were isolated from whole human blood (Biological Specialty Corp., Colmar, PA, USA) by centrifugating them twice in cold (4 °C) isotonic phosphate-buffered saline (defined as  $1\times$  PBS;  $\sim 310$  milliosmoles (mOsm)). Isolated RBCs were then subjected to hypotonic  $0.25\times$  PBS ( $\sim 80$  mOsm) treatment to remove the hemoglobin content of the cells, followed by centrifugation (20,000  $\times g$ , 20 min, 4 °C) with the supernatant discarded after each wash. Hypotonic treatment was repeated until an opaque white pellet was obtained, indicating the formation of micro-sized erythrocyte ghosts ( $\mu$ EGs) with completely or partially removed hemoglobin.

To form nano-sized EGs (nEGs),  $\mu EGs$  were extruded sequentially through 800-, 400-, and 200-nm polycarbonate porous membranes (Sterlitech Corp., Kent, WA, USA) using a 10 mL extruder (LIPEX®, TRANSFERRA Nanosciences Inc., Burnaby, B.C., Canada) at least three times through each membrane. These nEGs were then incubated in the loading solution containing equal volumes of nEGs suspended in  $1\times$  PBS, 0.1 M Sørenson's buffer (Na<sub>2</sub>HPO<sub>4</sub>/NaH<sub>2</sub>PO<sub>4</sub>,  $\sim$ 140 mOsm, pH  $\sim$ 7.4), and ICG dissolved in water. The final concentration of ICG in the loading buffer was 15  $\mu$ M. The solution was then centrifuged (100,000  $\times$ g, 1 h, 4  $^{\circ}$ C) and washed twice in  $1\times$  PBS to remove any excess ICG. The resulting nNETs pellets were suspended in  $1\times$  PBS.

To form cholesterol-enriched nNETs, referred to as  $C^+$ nNETs,  $\mu$ EGs were incubated in isotonic PBS containing cholesterol-Methyl- $\beta$ -cyclodextrin (M $\beta$ CD) complex (Sigma-Aldrich) at 37 °C for 1 h before and after the extrusion process. The cholesterol concentration was 15 mM as we had previously determined that this concentration imparted the maximum level of cholesterol to the membrane of  $\mu$ EGs. <sup>29</sup> Particles were then washed twice to remove any excess cholesterol. Cholesterol-enriched  $\mu$ EGs were then extruded as above, enriched with cholesterol again, and followed by incubation in the loading buffer containing 15  $\mu$ M ICG.

To functionalize the nanoparticles with FA, we mixed 1 mg/mL of 1,2-distearoyl-sn-glycero-3-phosphoethanolamine (DSPE)-polyethylene glycol (PEG) (2000 Da) (DSPE-PEG-FA, Nanosoft Polymers, Winston-Salem, NC, USA) with µEGs (as prepared above) in isotonic PBS prior to the extrusion process. This process results in insertion of the DSPE component into the lipid phase of the  $\mu EGs$ . After extrusion, the resulting nEGs were incubated in the loading buffer containing 15 µM ICG to from nNETs functionalized with FA (referred to as F-nNETs). To fabricate F-nNETs enriched with cholesterol (referred to F-C<sup>+</sup>nNETs), μEGs were incubated simultaneously with both DSPE-PEG-FA linker (1 mg/mL) and cholesterol-MβCD complex (15 mM cholesterol) in isotonic  $1 \times$  PBS at 37 °C for 1 h before the extrusion process. After extrusion, the particles were incubated with cholesterol-MβCD complex again, and then washed twice in 1 × PBS followed by centrifugation (100,000  $\times$ g, 1 h, 4 °C). Lastly, these particles were loaded with ICG using the same process above to from F-C<sup>+</sup>nNETs.

## Physical and optical characterization of nano-constructs

Membrane cholesterol content of the nano-constructs suspended in 1  $\times$  PBS was quantified using the Amplex Red Cholesterol Assay Kit (Invitrogen Molecular Probes) as described previously.  $^{29}$  Briefly, we oxidized membrane-bound cholesterol with cholesterol oxidase to produce  $\rm H_2O_2$ , which can be detected by the Amplex Red reagent. The reagent then reacts with  $\rm H_2O_2$  in the presence of horseradish peroxidase producing a highly fluorescent resorufin with respective absorption and emission maxima at 571 nm and 585 nm. We photo-excited the resorufin at  $\rm 560 \pm 2.0$  nm and obtained the emission recorded at 590 nm using a microplate reader (SpectraMax m3 microplate reader). Amount of cholesterol present in each sample was quantified by comparing the recorded emission values to a cholesterol standard curve that related the fluorescence emission at the same wavelength to various concentrations of cholesterol in the reaction buffer.

The zeta potentials and hydrodynamic diameters of the nanoconstructs suspended in 1  $\times$  PBS were measured by dynamic light scattering (DLS) (Zetasizer Nanoseries, NanoZS90, Malvern Instruments). We used lognormal functions to fit the DLS-based estimates of the hydrodynamic diameters of the nano-constructs. Absorption spectra were recorded using a UV–Vis spectrophotometer (Jasco-V670 UV–Vis spectrometer, JASCO) with optical path length of 1 cm. Fluorescence emission spectra of the nanoparticles in response to photoexcitation at 720  $\pm$  2.5 nm filtered from a 450-W xenon lamp were acquired using a fluorometer (Fluorolog-3 spectrofluorometer, Edison). Fluorescence emission from FA in response to photo-excitation at 350  $\pm$  2.5 nm was recorded in the spectral range of 365–900 nm. The

normalized the fluorescence emission  $\gamma(\lambda)$  spectra were obtained as:

$$\chi(\lambda) = \frac{F(\lambda)}{1 - 10^{-A(\lambda_{\rm ex})}}\tag{1}$$

where F is the fluorescence emission intensity in response to the excitation wavelength ( $\lambda_{ex}$ ), and  $A(\lambda_{ex})$  is the absorbance of the sample at  $\lambda_{ex}$ .

#### Flow cytometry

To quantify the percentage of the nano-constructs populations positive for PS, we used the annexin V-Alexa Flour 88 conjugate (AV-AF488) (Thermo Fisher Scientific) as the detection reagent. Approximately 0.5  $\mu L$  of RBCs, nano-sized RBCs (nRBCs) formed by extrusion as described above, nEGs, or cholesterol-enriched nEGs (C $^+$ nEGs) formed using 20 mM cholesterol complexed with M $\beta$ CD were incubated in 500  $\mu L$  of annexin binding buffer (10 mM HEPES, 140 mM NaCl, 2.5 mM CaCl $_2$  dissolved in water) (Thermo Fisher Scientific), followed by addition of 40  $\mu L$  of AV-AF488, for 20 min at 22  $^{\circ}$ C prior to flow cytometry analysis (LSR II, BD Biosciences).

For the analysis of the flow cytometry data, we used forward scattering area versus side scattering area plots to identify the population of particles, and used the FITC channel (488  $\pm$  2 nm photo-excitation, 530  $\pm$  nm fluorescence emission filter to identify the particles positive for PS). Fluorescence gating was done by juxtaposing the fluorescence of AV-AF488 stained samples against unstained samples. We also determined the change in mean fluorescence intensity ( $\Delta$ MFI) of the stained samples using the FITC channel.

#### SKOV3 cell culture

SKOV3 ovarian cancer cells (ATCC, Manassas, VA, USA) were used for tumor implantation in Nu/J female nude mice. Cells were cultured in Roswell Park Memorial Institute (RPMI) 1640 medium (Mediatech Inc., Manassas, VA, USA) containing 10 % fetal bovine serum (FBS) and 1 % penicillin/streptomycin (Corning Inc., Corning, NY, USA) at 37  $^{\circ}\text{C}$  in 5 % humidified CO2 incubator.

## In vitro phagocytosis

We used RAW264.7 murine macrophages to evaluate the uptake dynamics of nNETs and C<sup>+</sup>nNETs. Approximately  $10^6$  cells were seeded per well in a 96-well plate, and incubated with 100  $\mu L$  of Dulbecco's modified Eagle's medium (DMEM) supplemented with 10 % fetal bovine serum and 1 % penicillin/streptomycin for 24 h at 37 °C with 5 % CO2. Following this initial incubation, the original DMEM containing serum was removed, and the cells were then incubated with 50  $\mu L$  of serum-free DMEM mixed with 50  $\mu L$  of each sample at 37 °C for 30, 60, and 120 min

At each time point, we washed the cells with isotonic PBS to remove the non-engulfed particles. The cells were fixed with 4 % paraformaldehyde, permeabilized with 2 % Tween, and stained with 4′,6-diamidino-2-phenylindole (DAPI). They were then fluorescently imaged using an inverted microscope (Eclipse Ti, Nicken) with a NIR filter set at 740  $\pm$  18 nm photo-excitation and a long-pass filter (> 780 nm) (41037-Li-Cor IR800, Chroma Technology Corp.) as the ICG (red) channel. Fluorescence emission from DAPI (blue channel) at 477  $\pm$  30 nm was recorded in response to photo-excitation at 377  $\pm$  25 nm. We then obtained the average emission intensity per cell by summing the NIR emission intensity values for all pixels in a given image, dividing the sum by the number of cells in a given image, and finally averaging among the number of images acquired from cells incubated with either nNETs or  $\rm C^+ nNETs$  at each of the incubation time points.

#### Animal studies

Female Nu/J mice (20–25 g, 6–8 weeks) were purchased from Jackson Laboratory (Bar Harbor, Maine, USA). Animal studies were performed under a protocol approved by the University of California, Riverside Institutional Animal Care and Use Committee (protocol A-20200027). Animals were anesthetized by inhalation of 2 % isoflurane in oxygen. Each mouse was injected with  $\sim\!\!2\times10^7$  SKOV3 cells intraperitoneally. Mice were monitored until tumor growth was expected (~18 days).

Tumor-bearing mice were randomly divided into five groups with three animals in each group. Animals in each group received 100  $\mu L$  of either free ICG (15  $\mu M$ ) or the various types of nanoparticles (nNETs, F-nNETs, C+nNETs and F-C+nNETs) by tail vein injection under anesthesia. The injected dosages of ICG were estimated to be  $\sim\!58$  and 22.6–28.5  $\mu g/kg$  weight of the mouse ( $\sim\!20$  g) for free ICG and the nanoparticles variants, respectively. We note that these dosages are much lower than the LD50 values of  $\sim\!62$  mg/kg in mice $^{32}$  and 2 mg/kg in humans recommended by FDA. Mice were euthanized by inhalation of compressed CO2 gas at 24 h post-injection of the agents. Following euthanasia, we collected  $\sim\!500$   $\mu L$  of blood by cardiac puncture and extracted the liver, spleen, kidneys, lungs, heart, intestine, and tumors to fluorescently image them, and quantify the ICG content.

## Fluorescence imaging of extracted organs

Extracted organs were imaged in a luminescence dark box as our previously published study.  $^{33}$  Briefly, NIR fluorescence emission from extracted organs in response to 700  $\pm$  30 nm excitation from light emitting diodes was filtered using a long pass filter transmitting wavelengths >810 nm, and recorded by a charge-coupled device (CCD) camera (Pixis 1024B, Roper Scientific, Trenton, NJ, USA) with exposure time set as 90 s. We analyzed the acquired images using the ImageJ software, and present the mean intensity values  $\bar{(I)}$  from selected regions of interest (ROIs) for each organ and tumor as follows:

$$\bar{I} = \frac{\sum_{k=1}^{n} \left(\frac{1}{m_k}\right) \left[\left(\frac{1}{p}\right) \sum_{j=1}^{p} I_j\right]}{n} \tag{2}$$

where  $I_j$  is the pixel intensity at the  $j^{th}$  pixel of a given image, n and m are the number and mass of a given organ or tumor, respectively, and p is the total number of pixels in the ROI.

## Analysis of ICG content in blood, tumors, and organs

To measure the ICG content in the extracted blood samples, the blood was first weighed and then mixed with 700 µL of 5 % sodium dodecyl sulfate (SDS) (Sigma Aldrich, St. Louis, MO, USA) to lyse the nanoparticles, thus releasing the ICG. The samples were incubated at 4 °C for 30 min, followed by centrifugation (15,000 ×g, 1 h, 4 °C). The supernatant was then collected for fluorescence measurements. For organ and tumor analysis, each extracted organ or tumor was weighed and incubated in 1 mL of 5 % SDS at room temperature (RT) for 30 min in the dark. The organs and tumors were then grinded using a tissue homogenizer (Omni TH115, Omni International Inc., Kennesaw, GA, USA). We added another 3 mL of 5 % SDS to the homogenate and incubated it at RT for 30 min in the dark. After the incubation, the homogenate was centrifuged at 14,000  $\times g$  for 45 min at 10 °C. We then collected 1 mL of the supernatant containing ICG from each tube for fluorescence measurements. For both blood, and homogenized organs and tumors, the fluorescence emission in the range of 735–900 nm in response to 720  $\pm$ 2.5 nm photo-excitation wavelength was recorded using the Fluorolog-3 spectrofluorometer. Fluorescence spectra were fitted with Gaussian functions. We present the percentage of ICG recovered from each organ, tumor, or blood sample with respect to the initial injected dose per milligram of the sample (%ID mg<sup>-1</sup>). We used t-test (two-tailed) statistical analysis to compare the means of any two populations of interest.

#### Results and discussion

#### Characterizations

As determined by fitting the lognormal functions to the DLS-based measurements, the average hydrodynamic diameters  $\pm$  standard deviation (SD) of nNETs, F-nNETs, C+nNETs, and F-C+nNETs suspended in isotonic PBS were 129.51  $\pm$  0.76, 131.64  $\pm$  0.18, 118.54  $\pm$  0.59, and 219.2  $\pm$  0.79 nm, respectively (Fig. 2A). The respective mean  $\pm$  SD values of zeta potentials for nNETs, F-nNETs, C<sup>+</sup>nNETs, and F- C<sup>+</sup>nNETs in isotonic PBS were  $-12.8 \pm 0.1$ ,  $-10.27 \pm 1.2$ ,  $-10.77 \pm 0.38$ , and - $10.16 \pm 0.32$  mV (Fig. 2B). We suggest that the negative values of the zeta potentials are attributed to the sialoglycoproteins, the primary negative charge-bearing components of the RBC membrane. The mean zeta potential for nNETs was significantly lower (p < 0.05) as compared to the values for the other nano-constructs, suggesting that FA functionalization and cholesterol enrichment of the particles resulted in a slight but statistically significant increase (less negative value) in the zeta potential. These results are consistent with those reported in literature where functionalization of Fe<sub>3</sub>O<sub>4</sub> nanoparticles with FA shifted the zeta potential to more positive values,<sup>34</sup> as well as our previous study where F-NETs utilized to induce photothermal destruction of tumors, had a more positive zeta potential ( $-12.68 \pm 0.64$  mV) as compared to nNETs  $(-14.52 \pm 1.39 \text{ mV})$ . 35

Illustrative absorption spectra of nNETs, F-nNETs, C<sup>+</sup>nNETs, and F-C<sup>+</sup>nNETs suspensions in 1  $\times$  PBS are shown in Fig. 2C. All nanoparticles present a spectral peak at  $\sim\!802$  nm, which corresponds to the monomeric form of ICG,  $^{19,36}$  indicating successful encapsulation of ICG in these constructs. We suggest that the lower absorbance value at  $\sim\!802$  nm for F-nNETs is attributed to the lower loading efficiency of ICG as compared to nNETs and C<sup>+</sup>nNETs. The lower absorbance value at 280 nm for F- C<sup>+</sup>nNETs suggests that fewer of these particles were formed as compared to nNETs and F-nNETs. The fluorescence emission peaks at  $\sim\!809$  nm (Fig. 2D) and  $\sim$  442 nm (Fig. 2E) are associated with the presence of ICG and FA, respectively. The most intense NIR emission spectrum was associated with nNETs (Fig. 2D), suggesting higher amounts of ICG were loaded into these particles, and/or greater number of these particles were formed.

The cholesterol level in each nano-construct type relative to the amount in RBCs is shown in Fig. 2F. The membrane cholesterol content of nNETs was lower by about twofold as compared to RBCs (p < 0.001), which may have resulted from losing some of the RBCs during the fabrication process. There was a statistically significant increase of approximately 1.5fold in the relative cholesterol content in C<sup>+</sup>nNETs as compared with nNETs (p < 0.001). The relative cholesterol content of FC<sup>+</sup>nNETs was significantly higher as compared to the other nanoconstructs and RBCs. One possible reason for increased cholesterol level of F-C<sup>+</sup>nNETs is that the membrane-anchored DSPE-PEG-Folate linker may alter the packing of the phospholipids in the bilayer to accommodate additional cholesterol.

Flow cytometry results demonstrate the effectiveness of membrane cholesterol enrichment in lowering PS externalization of RBC-derived nano-constructs (Fig. 3). Nano-sized RBCs exhibited a population fraction of 15.9 % that were positive for PS externalization (Fig. 3A), which we attribute to the extrusion of the RBCs. The population fraction of nEGs that were positive for PS externalization was 27.1 % (Fig. 3B). The higher PS $^+$  fraction of nEGs is likely due to the combined effects of hypotonic treatment of the RBCs followed by the extrusion process.

The population fraction of  $C^+$ nEGs positive for PS was 13.2 % (Fig. 3C), demonstrating that membrane cholesterol enrichment was effective in reducing PS externalization. Native RBCs without any manipulation showed minimal change in their mean fluorescence intensity ( $\Delta$ MFI) (Fig. 3D), indicating that PS was minimally externalized

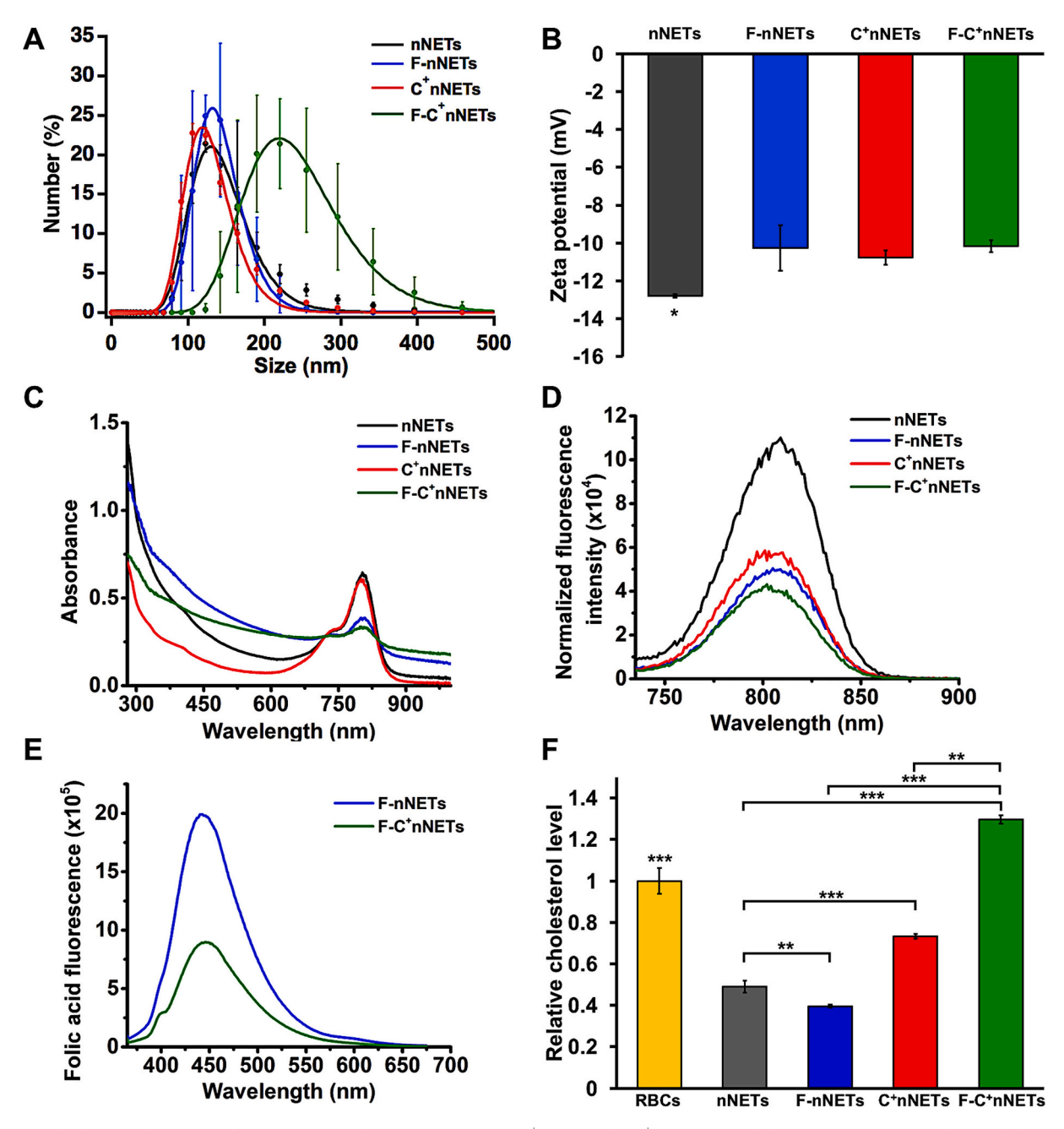
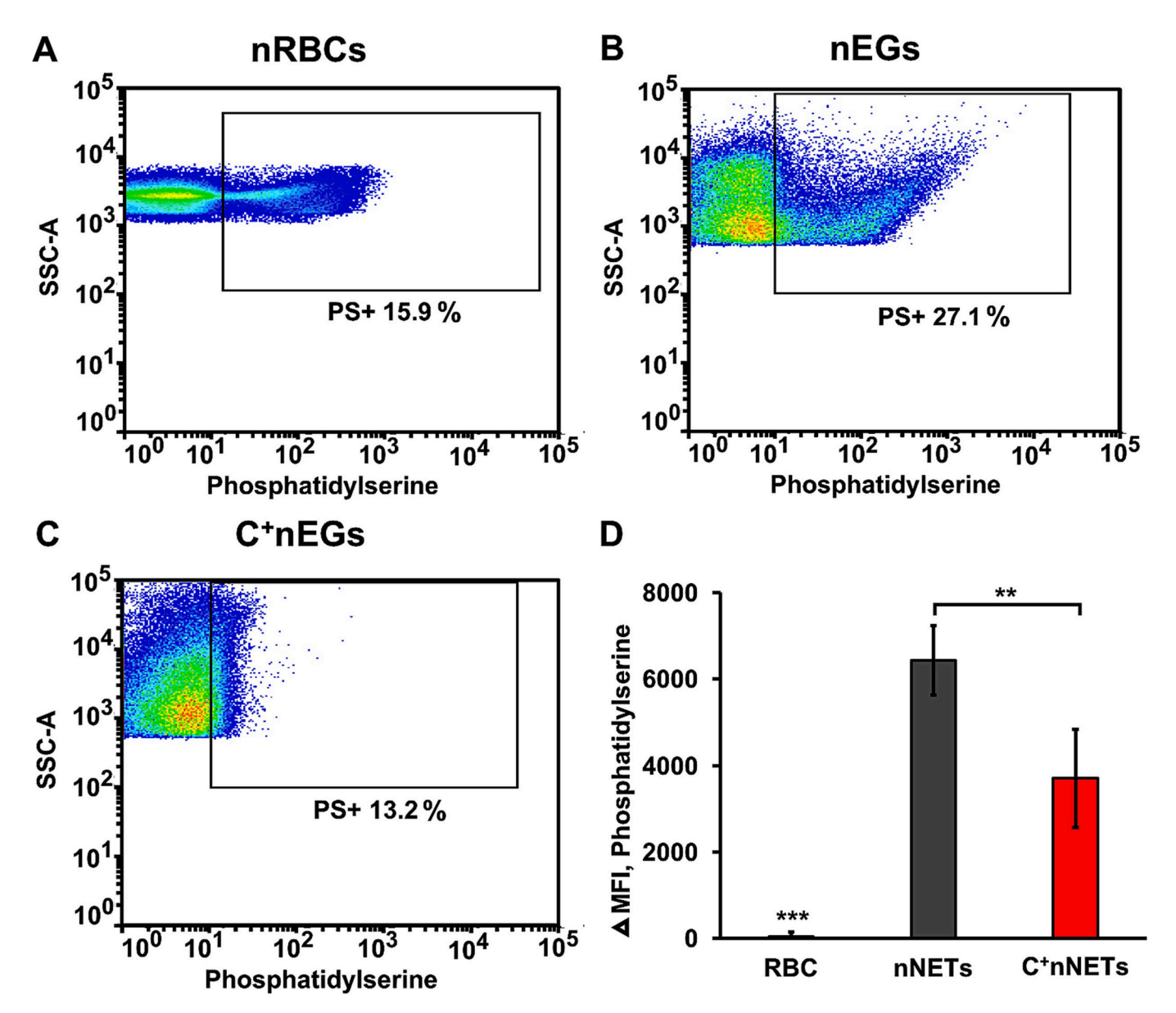


Fig. 2. (A) Hydrodynamic diameters and (B) zeta potentials of nNETs, F-nNETs and F-C<sup>+</sup>nNETs suspended in isotonic PBS. In panel (A), solid traces are the lognormal fits to the mean values of DLS-based measurements of the hydrodynamic diameters as represented by various symbols. Three independent measurements were used to obtain the mean values of the hydrodynamic diameters and zeta potentials. (C) Absorption and (D) Normalized fluorescence emission spectra in response to  $720 \pm 2.5$  nm photo-excitation. (E) Folic acid fluorescence spectra in response to  $350 \pm 2.5$  nm photo-excitation of F-nNETs, and F-C<sup>+</sup>nNETs. (F) Mean values of the relative membrane cholesterol level of various nano-constructs based on four independent measurements. Error bars in panels (B) and (F) represent standard deviations from the mean. Asterisks \*, \*\*, and \*\*\* define statistically significant differences at p < 0.05, p < 0.01, and p < 0.001, respectively. In panels (B) and (F), the mean values for RBCs were significantly different as compared to the values for all nano-constructs.



**Fig. 3.** Flow cytometry-based detection of PS. Representative dot plots of side scattering area (SSC-A) versus fluorescently-detected PS for (A) nRBCs, (B) nEGs, and (C)  $C^+$ nEGs are presented. In panel (D), the change in mean fluorescence intensity of AV-AF488 labeled PS for RBCs, nEGs, and  $C^+$ nEGs are shown. Asterisks \*\*\* and \*\* indicate statistically significant differences at p < 0.001 and p < 0.01, respectively.

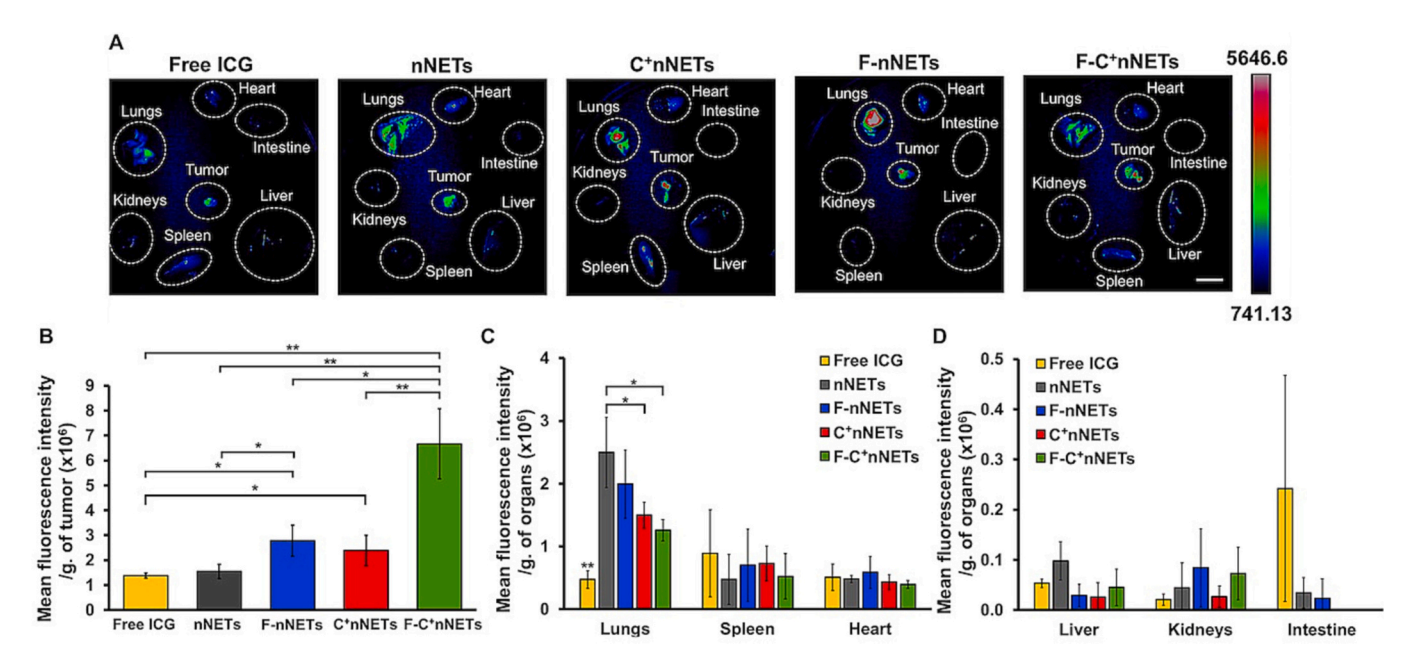


Fig. 4. (A) Representative NIR fluorescence images of organs and tumors extracted at 24 h post tail-vein injection of free ICG, nNETs, F-nNETs, C<sup>+</sup>nNETs, and F-C<sup>+</sup>nNETs from Nu/J mice. Excitation wavelength =  $700 \pm 3$  nm. Emission >800 nm was collected. Scale bar on the right represents the fluorescence emission intensity. Scale bar on the image equals 5 mm and applies to all panels. Mean  $\pm$  standard deviation in fluorescence intensity per mass of (B) tumors, (C) and (D) extracted organs. Note that panels (B)-(D) have different scales. n = 3 per agent. Asterisks \* and \*\* correspond to statistically significant differences with p < 0.05 and p < 0.01, respectively, between the indicated pairs. In panel (C), \*\* for free ICG indicates that its mean intensity value in lungs was significantly different as compared to the values for other agents (p < 0.01).

in RBCs. Upon membrane cholesterol enrichment,  $\Delta$ MFI of C<sup>+</sup>nNETs became significantly lower (p < 0.01) as compared to the value for nNETs.

## Fluorescence imaging of extracted organs

We performed in vivo experiments to evaluate the tumor accumulating ability of each of the nano-constructs and free ICG, and their biodistributions in Nu/J nude mice. Representative fluorescence images and quantitative NIR fluorescence emission characterizations from extracted organs of mice at 24 h post-injection of the various agents are shown in Fig. 4. Fluorescence images demonstrated that in addition to the lungs, spleen, and heart, all agents had accumulated in tumors (Fig. 4A). Previously, we reported that enriching the membrane of RBCderived micro-particles with cholesterol prolonged the circulation time of the particles.<sup>29</sup> Herein, our quantitative analysis of the fluorescence images, based on Eq. (2), indicates that the mean NIR emission intensity of C<sup>+</sup>nNETs from tumors was ~54 % greater than that of nNETs at 24 h post-injection (Fig. 4B), suggesting that membrane cholesterol enrichment was an effective method to increase the accumulation of the particles in tumors. Administration of F-C<sup>+</sup>nNETs produced significantly higher mean emission intensity per gram of tumor as compared to other nano-constructs and free ICG (Fig. 4B). In particular, at 24 h postinjection, the mean emission intensity associated with accumulation of F-C<sup>+</sup>nNETs in tumors was ~2.8fold and 2.4fold higher than those associated with C+nNETs and F-nNETs, respectively. These results suggest that functionalizing the C+nNETs with FA increases the accumulation of the particles in tumors in addition to what can be offered by membrane cholesterol enrichment or FA functionalization alone.

The liver, spleen and lungs are the primary organs of reticuloendothelial system (RES) to eliminate foreign materials.<sup>37</sup> The greatest mean

emission intensity from all nano-constructs was detected in the lungs (Fig. 4C). Lungs have abundant alveolar macrophages<sup>38</sup> to entrap particles and clear them from the body. Among all administered nano-constructs, nNETs showed the highest NIR signal from the lungs (Fig. 4C) while exhibiting the lowest signal from tumors (Fig. 4B) at 24 h post-injection, suggesting that these nano-constructs were the least effective in tumor imaging. As compared to the NIR fluorescence signal from the tumors associated with administration of F-C<sup>+</sup>nNETs (Fig. 4B), the signals emanating from the lungs, spleen, and liver were lower (Fig. 4C&D), indicating F-C<sup>+</sup>nNETs had accumulated in tumors at higher quantities as compared to the RES organs.

Analysis of ICG content in blood and within homogenized tumors and organs

To evaluate the effects of cholesterol enrichment and folate functionalization on blood content, tumor accumulation, and biodistribution of the nano-constructs, we analyzed the NIR fluorescence emission spectra of blood, tumors, and organs from mice at 24 h post-tail vein injection of the various nanoparticles, and compared them with those for free ICG. There was negligible emission from the blood of mice injected with free ICG (Fig. 5A), indicating that ICG has cleared from the vasculature at 24 h post-injection. C<sup>+</sup>nNETs showed the highest fluorescence emission intensity as compared to other nano-constructs (Fig. 5A), suggesting that membrane cholesterol enrichment was effective in prolonging the circulation time of the nanoparticles.

We used the integrated NIR fluorescence emission over the 735–900 nm band normalized by the mass of the blood, tumors, and various organs as a metric related to the quantity of ICG present as free or encapsulated form within each of the nano-constructs (Fig. 5B). The mean value of this metric for C<sup>+</sup>nNETs in blood was significantly greater

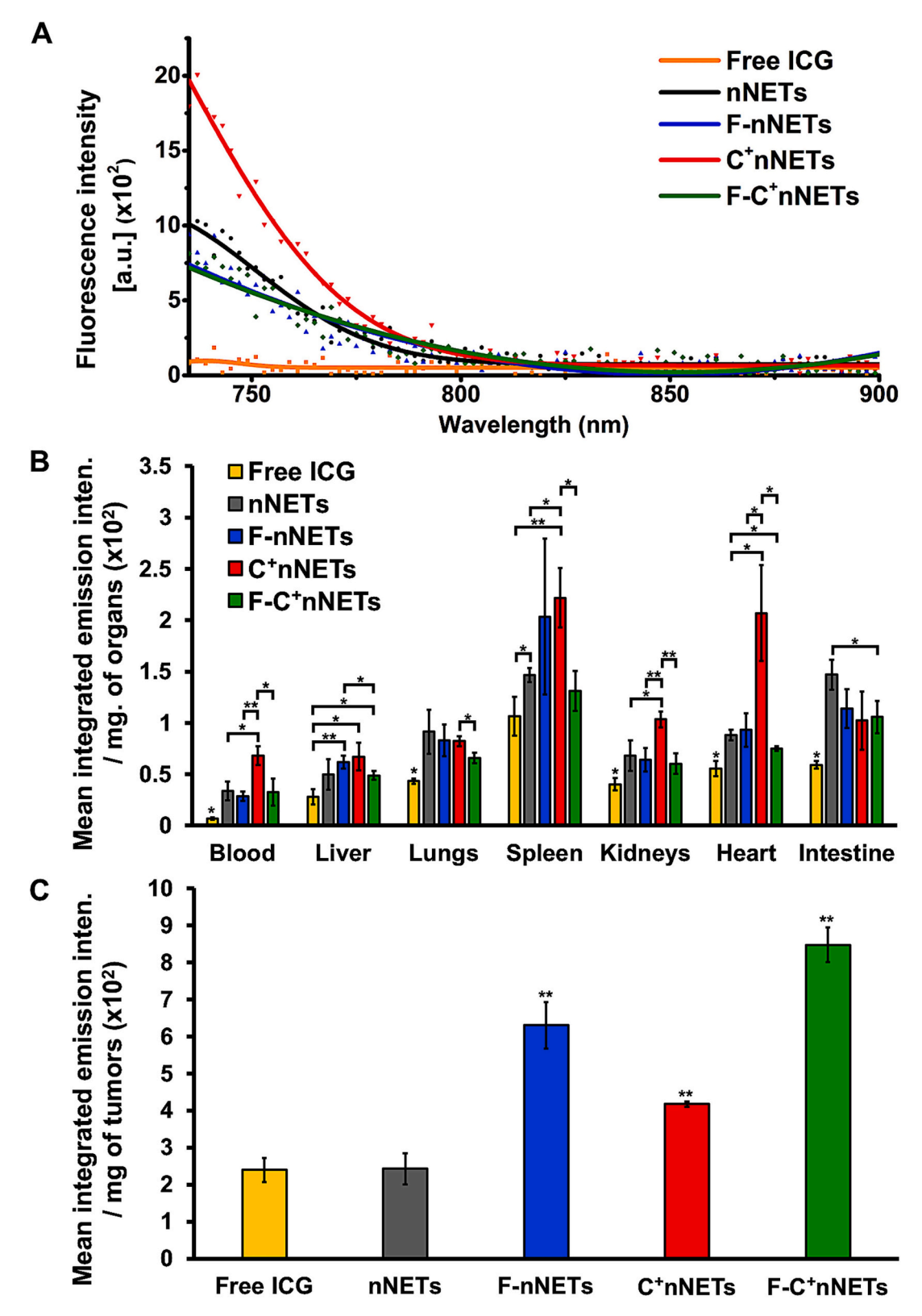
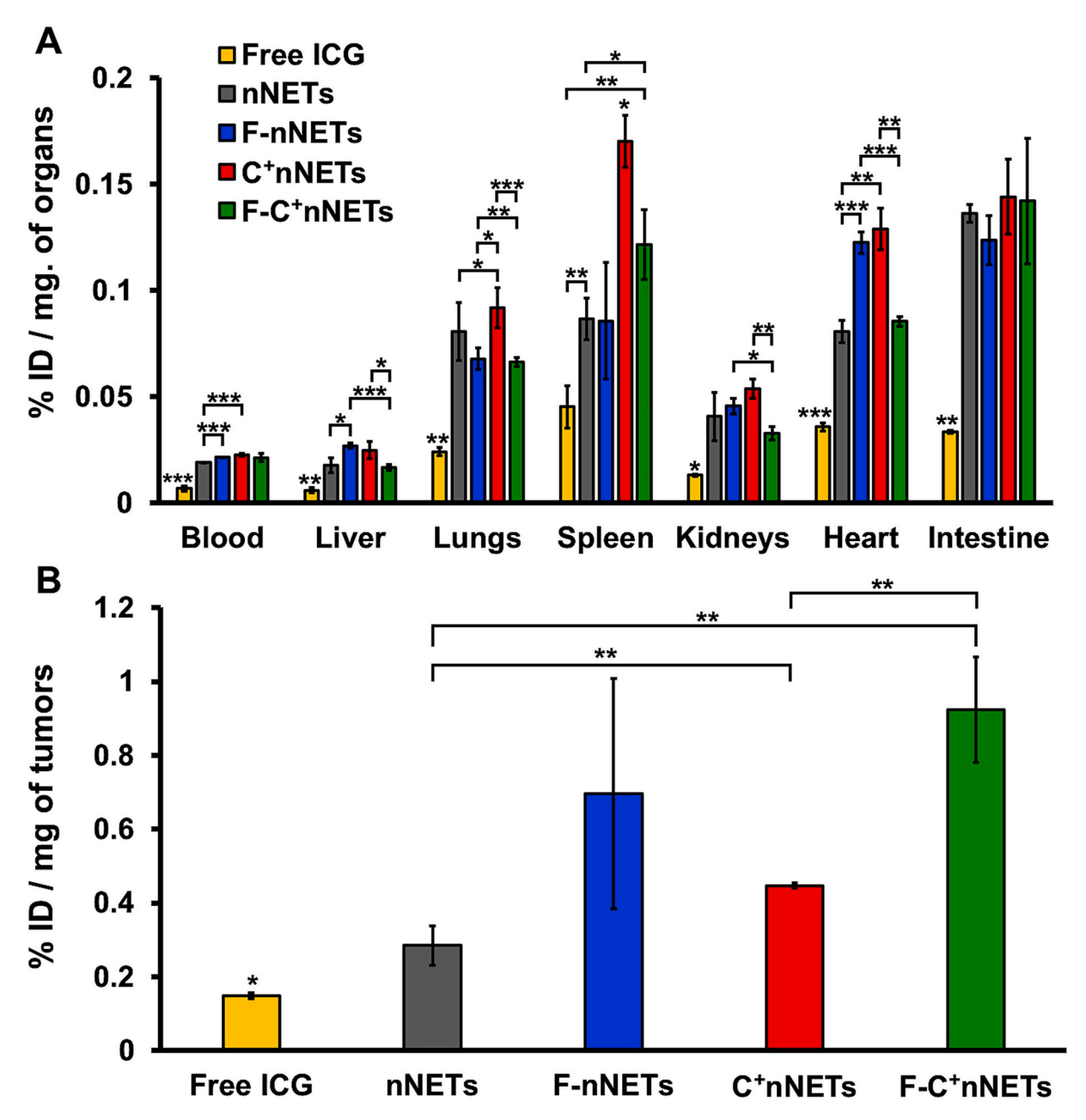


Fig. 5. (A) Fluorescence emission spectra of blood collected from mice at 24 h following tail-vein injection of free ICG and various nano-constructs in response to 720  $\pm$  2.5 nm photo-excitation. Solid traces are Gaussian fits to the data points. Mean values of the spectrally integrated emission intensity of blood and homogenized organs (B) and (C) tumors normalized to the mass of the blood/organs or tumors collected from three mice for each administered agent. Asterisks denote statistically significant differences between the indicated pairs (\*, p < 0.05; \*\*, p < 0.01). In panel (B), \* above the bar for free ICG indicates that its mean intensity value was significantly different as compared to the values for other agents (p < 0.05). In panel (C), \*\* above the indicated agents imply that there was a significant different in the mean value between that agent and every other agent with p < 0.01. Note that panels (B) and (C) have different scales.



**Fig. 6.** Recovered percentage of the initial dose of ICG normalized to the mass of extracted blood and organs (A) and tumors (B) (% ID/ mg) at 24 h post-injection of various agents. n = 3 animals per administered agent. Error bars represent standard deviations from the mean. In panel (A), \*,\*\*,\*\*\* above the indicated agents imply that there was a statistically significant difference in the mean value between that agent and every other agent with p < 0.05, p < 0.01 or p < 0.001, respectively. In panel (B), the single asterisk above ICG indicates that its associated mean value was significantly lower (p < 0.05) as compared with those for all other agents. Other remaining asterisks denote statistically significant differences between the indicated pairs (\*\*, p < 0.01). Note that panels (A) and (B) have different scales.

than that of other particles types at 24 h time point; however, there were no statistically significant differences among the values for nNETs, F-NETs, and F- C+nNETs (Fig. 5B). One explanation for this result is that the insertion of the DSPE-PEG-Folate linker into the bilayer may induce redistribution of the various phospholipids, and in particular, the flipping of some of the PSs to the outer leaflet of the membrane, serving as a signal to the macrophages for removal of the nano-constructs functionalized with FA. In all organs, and particularly in the liver and the intestine, the average mass-normalized integrated fluorescence of free ICG was significantly lower than all nano-constructs (Fig. 5B), suggesting that a higher fraction of ICG had been eliminated from the body through the hepatobiliary mechanism. Similarly, for nNETs, a relatively large value of the mass-normalized emission was with associated with the intestine, suggesting that some fraction of nNETs was in the process

of elimination from the body at 24 h pos-injection time. Greatest fluorescence emission from the highly vascularized organs of liver, spleen, kidneys and the heart were associated with  $C^+ n N E T s$  as compared to other agents (Fig. 5B). These results suggest the membrane cholesterol enrichment alone was a contributing factor to mediate the greatest availability of  $C^+ n N E T s$  in these highly vascularized organs as a result of prolonged circulation.

Analysis of homogenized tumors revealed that the average mass-normalized integrated fluorescence of C<sup>+</sup>nNETs was significantly higher as compared to that of free ICG and nNETs (p < 0.01), but lower as compared to F-NETs and F- C<sup>+</sup>nNETs at 24 h time point (Fig. 5C). The average mass-normalized integrated fluorescence from tumors associated with administration of F-C<sup>+</sup>nNETs was significantly higher (p < 0.01) as compared to all other administered agents; in particular, this

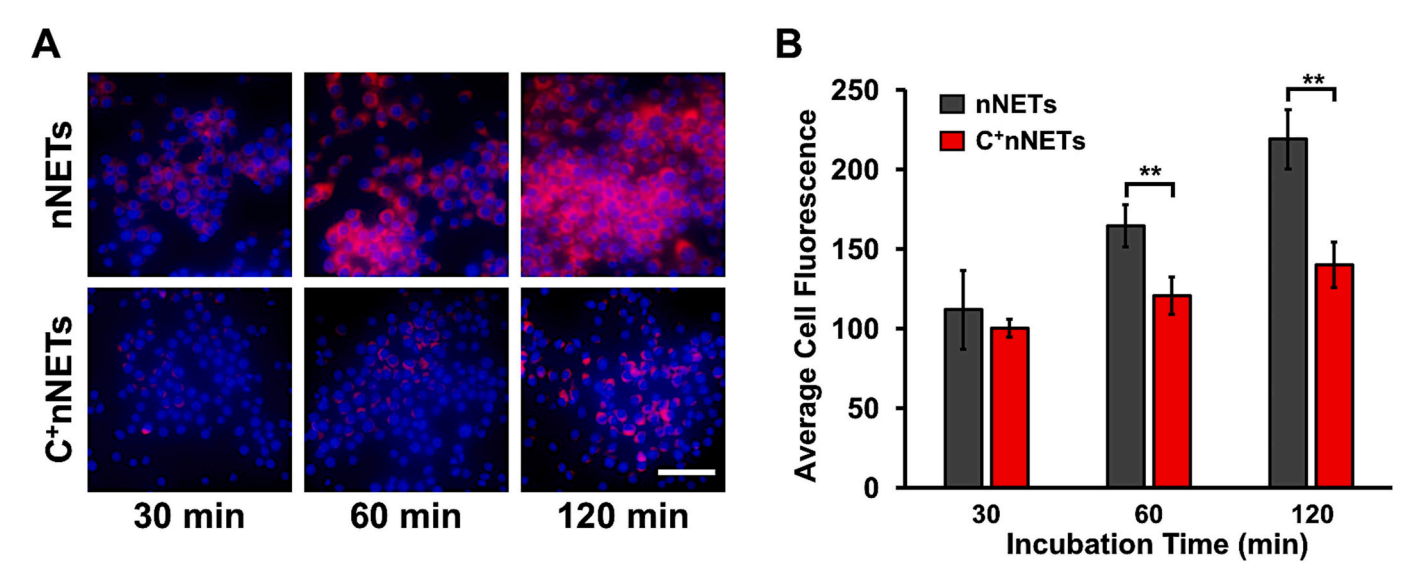


Fig. 7. In vitro uptake dynamics of nNETs and  $C^+$ nNETs by RAW 264.7 murine macrophages. (A) Fluorescence images of macrophages after 30, 60, and 120 min of incubation with nNETs (top row) and  $C^+$ nNETs (bottom row). Scale bar = 50  $\mu$ m and applies to all images. (B) Average NIR emission intensity per macrophage after 30, 60, and 120 min of incubation with nNETs and  $C^+$ nNETs. Error bars are standard deviations from the mean. Asterisks \*\* indicate statistically significant differences in the average emission intensity between the indicated pairs.

was value was  ${\sim}35$  % and  ${\sim}103$  % higher as compared to F-nNETs and  $C^+$ nNETs, respectively. These results demonstrate that while either functionalization with FA or cholesterol enrichment of nNETs resulted in increased fluorescence from tumors, the combination of FA functionalization and cholesterol enrichment had a synergistic effect to further increase fluorescence emission from tumors.

Concomitant with the lower fluorescence emission of F-nNETs and F-C<sup>+</sup>nNETs from the liver, spleen, and kidneys as compared to C<sup>+</sup>nNETs (Fig. 5B), F-nNETs and F-C<sup>+</sup>nNETs exhibited higher fluorescence from tumors at 24 h post-injection (Fig. 5C). These results indicate that FA functionalization provided a capability for F-nNETs and F-C<sup>+</sup>nNETs to target the tumors more effectively despite some accumulation in other organs. When further combined with membrane cholesterol enrichment, there was a trend in reduced fluorescence emission in various organs resulting from administration of F-C<sup>+</sup>nNETs as compared to other nanoconstructs (Fig. 5B), while achieving significantly higher emission from the tumors (p < 0.01) (Fig. 5C).

We also quantified the biodistribution of particles in blood, and the extracted organs and tumors by calculating the percentage of the injected dose (ID) recovered per mass (%ID/mg) (Fig. 6). The massnormalized fraction of free ICG in the blood and all organs was significantly lower than all other agents, indicating that a higher fraction of free ICG had been cleared from the body at 24 h post-injection (Fig. 6A). Higher %ID/mg in the lungs and spleen was associated with C<sup>+</sup>nNETs as compared to other agents (Fig. 6A). The fraction of C<sup>+</sup>nNETs (0.45 %ID/ mg) in tumors was significantly higher than those of free ICG (0.15 %ID/ mg) and nNETs (0.28 %ID/mg) (Fig. 6B), which indicates the benefit of cholesterol enrichment in prolonging the circulation time so that a higher quantity of C<sup>+</sup>nNETs can remain available to reach the tumors. The higher fractions of F-nNETs (0.69 %ID/mg) and F-C<sup>+</sup>nNETs (0.92 % ID/mg) as compared to C<sup>+</sup>nNETs can be attributed to FA functionalization of the particles. However, there was about 33 % increase in %ID/ mg of F-C<sup>+</sup>nNETs in tumors as compared to F-nNETs, indicating the synergistic effects of cholesterol enrichment and FA functionalization for increased tumor targeting.

## Macrophage interactions

The lowered uptake rate of C<sup>+</sup>nNETs by macrophages provides a mechanism for the prolonged circulation of these particles. Our in vitro

results provide some evidence towards this mechanism. As the incubation time of RAW 264.7 murine macrophages with nNETs increased to 60 and 120 min, there was progressively greater NIR fluorescence emission from the cells, whereas macrophages incubated with  $\mathrm{C^+}$ nNETs displayed minimal emission over the course of 120 min (Fig. 7A). Quantitative image analysis of the cells indicated that there were statistically significant (p < 0.01) lower emissions from macrophages incubated with  $\mathrm{C^+}$ nNETs as compared to nNETs at 60 and 120 min of incubation (Fig. 7B).

Materials approved or investigated under clinical trials for ovarian cancer

Currently, pafolacianine,  $^{39,40}$  also known as OTL38, remains as the only molecular probe with FDA approval status (2021) for optical imaging of ovarian cancer. OTL38 is related to ICG, with similar fluorescence characteristics, in which the polyene bridge of ICG is split in the middle, and a cyclohexene is inserted in place and attached to folate for targeting FR- $\alpha$ . <sup>41</sup> Although the long-term benefits of OTL38 in terms of a reduction in recurrence and improved survival remain to be established, it is encouraging that fluorescence-guided resection of ovarian cancer is gaining clinical entry. Some of the shortcomings of OTL38 are its high false positive rates in the range of 32.7 %–56 %, <sup>39,42</sup> and emission from various anatomical sites. <sup>40</sup> Additionally, OTL38 has a relatively short half-life of ~21 min in bloodstream of mice. <sup>41</sup>

At this time, the only approved nanotechnology platforms in relation to ovarian cancer are Doxil and Apealea, which are used as chemotherapeutic agents. We provide a summary of various nanotechnology platforms that have been used in clinical trials for ovarian cancer imaging or therapy in Table 1. Currently, there are no approved nanotechnology platforms for optical imaging of ovarian cancer. A clinical trial using ONM-100, which consists of ICG molecules entrapped within micelles, was completed in 2021. The results of this clinical trial have not been published yet. The present study suggests that erythrocytederived nano-constructs with membrane cholesterol enrichment and FA functionalization may offer a potential nanotechnology platform for NIR fluorescence imaging of ovarian tumors.

## Ethics approval and consent to participate

All procedures involving laboratory animals were performed in

**Table 1**Nanotechnology platforms approved or used in clinical trials for ovarian cancer therapy or NIR fluorescence imaging.

Name	Nano-platform	Active agent/usage	Active targeting capability	Approval/investigational status	Illustrative publication
Apealea	Polymeric Micelle	Paclitaxel/ Therapy	No	EMA Approved (2018)	43
CriPec	Micelle	Docetaxel/	No	Clinical Trials:	44
		Therapy		NCT03742713	
				(Completed 2020-12-01)	
CRLX101	Cyclodextrin-PEG	Camptothecin	No	Clinical Trials:	45
(EP0057)				NCT01652079	
				(Completed 2018-03)	
				NCT04669002	
				(Completed 2023-08-02)	
Doxil	PEGylated	Doxorubicin/	No	FDA Approved (1995)	46
	Liposome	Therapy			
ELU001	PEGylated	Topoisomerase-1	Yes	Clinical Trials:	47
	Silica	Inhibitor (Exatecan),	(FR-α)	NCT05001282	
		Folic Acid/		(Active, Recruiting)	
		Therapy			
IMX-110	PEG-PE	Curcumin,	Yes	Clinical Trials:	47
	Micelle	Doxorubicin/	(Glucose Trasporter-1)	NCT03382340	
		Therapy	•	(Active, Not Recruiting)	
Irinotecan	Liposome	Irinotecan/	No	Clinical Trials:	48
Sucrosofate	1	Therapy		NCT04753216	
		17		(Completed 2021-10-25)	
Nab-	Albumin	Paclitaxel/	No	Clinical Trials:	49
Paclitaxel		Therapy			
				NCT00466960	
				(Completed 2011–07)	
				NCT00825201	
				(Completed 2018-01-16)	
				NCT00499252	
				(Completed 2011–07)	
				NCT03942068	
				(Completed 2020-12-30)	
				NCT03304210	
				(Completed 2020-05-06)	
				(Completed 2020-05-06)	
				NCT02762981	
				(Completed 2020-9-12)	
				NCT02020707	
				(Active, Not Recruiting)	
MT-302	Lipid	mRNA/	Yes	Clinical Trials:	50
	Lipid	Therapy	(TROP-2)	NCT05969041	
		тистару	(11(01-2)	(Active, Recruiting)	
ONM-100	Micelle	ICG/ Imaging	No	Clinical Trials:	51
	MICCIC	100/ magmg	110	NCT03735680	
				(Completed 2021-11-18)	
SNB-101	Micelle	Camptothecin/	No	Clinical Trials:	52
	whicehe	_	NO		
		Therapy		(Active, Recruiting)	

Abbreviations: FR-α: Folate receptor-alpha; ICG: Indocyanine green; PE: Phosphatidyl ethanolamine; PEG: Polyethylene glycol; TROP-2: Tumor-associated calcium signal transducer 2.

accordance with the guidelines of the Institutional Animal Care and Use Committee (under protocol A-20200027) at University of California, Riverside.

## Consent for publication

Not applicable.

## CRediT authorship contribution statement

Chi-Hua Lee: Experimental design, Animal experimentation, Data curation, Analysis and interpretation, Visualizations, Writing – original draft. Jenny Mac, Taylor Hanley, Raviraj Vankayala: Animal experimentations. Shamima Zaman: Data curation and analysis. Bahman Anvari: Conceptualization, Experimental design, Funding acquisition, Project administration, Supervision, Data analysis and interpretation, Validation, Writing – review and editing.

# Declaration of competing interest

In the past five years, author B.A. has a financial interest in Radoptics LLC, which is interested in pursuing the commercial development of the erythrocyte-derived particles. This interest did not interfere with the scientific work, judgement, or objectivity of the investigators with regards to the experimental procedures, analysis, reports, and interpretation of results, or any other aspects of the study. All remaining authors declare no conflicts of interest.

## Data availability

Add data generated or analyzed are included in this article.

## Acknowledgements

This study was supported in parts by a grant from the U.S. National Science Foundation (CBET-1940965).

#### References

- Siegel RL, Miller KD, Wagle NS, Jemal A. Cancer statistics, 2023. CA Cancer J Clin. 2023;73(1):17–48.
- Zivanovic O, Aldini A, Carlson JW, Chi DS. Advanced cytoreductive surgery: American perspective. Gynecol Oncol. 2009;114(2 Suppl):S3–S9.
- Bristow RE, Tomacruz RS, Armstrong DK, Trimble EL, Montz FJ. Survival effect of maximal cytoreductive surgery for advanced ovarian carcinoma during the platinum era: a meta-analysis. J Clin Oncol. 2002;20(5):1248–1259.
- Burns JM, Shafer E, Vankayala R, Kundra V, Anvari B. Near infrared fluorescence imaging of intraperitoneal ovarian tumors in mice using erythrocyte-derived optical nanoparticles and spatially-modulated illumination. *Cancers (Basel)*. 2021;13(11): 2544.
- Marshall MV, Rasmussen JC, Tan IC, Aldrich MB, Adams KE, Wang X, et al. Nearinfrared fluorescence imaging in humans with indocyanine green: a review and update. Open Surg Oncol J. 2010;2(2):12–25.
- Yannuzzi LA. Indocyanine green angiography: a perspective on use in the clinical setting. Am J Ophthalmol. 2011;151(5):745–751.
- 7. Tummers QR, Hoogstins CE, Peters AA, de Kroon CD, Trimbos JB, van de Velde CJ, et al. The value of intraoperative near-infrared fluorescence imaging based on enhanced permeability and retention of indocyanine green: feasibility and false-positives in ovarian cancer. PLoS One. 2015;10(6), e0129766.
- Desmettre T, Devoisselle JM, Mordon S. Fluorescence properties and metabolic features of indocyanine green (icg) as related to angiography. Surv Ophthalmol. 2000;45(1):15–27.
- Jia W, Burns JM, Villantay B, Tang JC, Vankayala R, Lertsakdadet B, et al. Intravital vascular photoheranostics and real-time circulation dynamics of micro- and nanosized erythrocyte-derived carriers. ACS Appl Mater Interfaces. 2020;12(1): 275–287.
- Meijer DK, Weert B, Vermeer GA. Pharmacokinetics of biliary excretion in man. Vi Indocyanine green. Eur J Clin Pharmacol. 1988;35(3):295–303.
- Yoneya S, Saito T, Komatsu Y, Koyama I, Takahashi K, Duvoll-Young J. Binding properties of indocyanine green in human blood. *Investig Ophthalmol Vis Sci.* 1998;39 (7):1286–1290.
- Cherrick GR, Stein SW, Leevy CM, Davidson CS. Indocyanine green: observations on its physical properties, plasma decay, and hepatic extraction. J Clin Investig. 1960;39 (4):592–600.
- Torchilin V. Tumor delivery of macromolecular drugs based on the epr effect. Adv Drug Deliv Rev. 2011;63(3):131–135.
- Peer D, Karp JM, Hong S, Farokhzad OC, Margalit R, Langer R. Nanocarriers as an emerging platform for cancer therapy. Nat Nanotechnol. 2007;2(12):751–760.
- Villa CH, Anselmo AC, Mitragotri S, Muzykantov V. Red blood cells: supercarriers for drugs, biologicals, and nanoparticles and inspiration for advanced delivery systems. Adv Drug Deliv Rev. 2016;106(Pt A):88–103.
- Burns JM, Vankayala R, Mac JT, Anvari B. Erythrocyte-derived theranostic nanoplatforms for near infrared fluorescence imaging and photodestruction of tumors. ACS Appl Mater Interfaces. 2018;10(33):27621–27630.
- Xia Q, Zhang Y, Li Z, Hou X, Feng N. Red blood cell membrane-camouflaged nanoparticles: a novel drug delivery system for antitumor application. *Acta Pharm Sin B*. 2019;9(4):675–689.
- Luo L, Zeng F, Xie J, Fan J, Xiao S, Wang Z, et al. A rbc membrane-camouflaged biomimetic nanoplatform for enhanced chemo-photothermal therapy of cervical cancer. J Mater Chem B. 2020;8(18):4080–4092.
- Bahmani B, Bacon D, Anvari B. Erythrocyte-derived photo-theranostic agents: hybrid nano-vesicles containing indocyanine green for near infrared imaging and therapeutic applications. Sci Rep. 2013;3:2180.
- Han X, Wang C, Liu Z. Red blood cells as smart delivery systems. Bioconjug Chem. 2018;29(4):852–860.
- Oldenborg PA, Zheleznyak A, Fang YF, Lagenaur CF, Gresham HD, Lindberg FP. Role of cd47 as a marker of self on red blood cells. *Science*. 2000;288(5473): 2051–2054.
- Makrides SC. Therapeutic inhibition of the complement system. Pharmacol Rev. 1998;50(1):59–87.
- Lee CH, Tang JC, Hendricks NG, Anvari B. Proteomes of micro- and nanosized carriers engineered from red blood cells. J Proteome Res. 2023;22(3):896–907.
- Arashiki N, Takakuwa Y. Maintenance and regulation of asymmetric phospholipid distribution in human erythrocyte membranes: implications for erythrocyte functions. Curr Opin Hematol. 2017;24(3):167–172.
- Schrier SL, Zachowski A, Herve P, Kader JC, Devaux PF. Transmembrane redistribution of phospholipids of the human red cell membrane during hypotonic hemolysis. *Biochim Biophys Acta*. 1992;1105(1):170–176.
- Kuypers FA, de Jong K. The role of phosphatidylserine in recognition and removal of erythrocytes. Cell Mol Biol (Noisy-le-Grand). 2004;50(2):147–158.
- Schroit AJ, Tanaka Y, Madsen J, Fidler IJ. The recognition of red blood cells by macrophages: role of phosphatidylserine and possible implications of membrane phospholipid asymmetry. *Biol Cell*. 1984;51(2):227–238.

- Wesseling MC, Wagner-Britz L, Huppert H, Hanf B, Hertz L, Nguyen DB, et al. Phosphatidylserine exposure in human red blood cells depending on cell age. *Cell Physiol Biochem*. 2016;38(4):1376–1390.
- Tang JC, Lee CH, Lu T, Vankayala R, Hanley T, Azubuogu C, et al. Membrane cholesterol enrichment of red blood cell-derived microparticles results in prolonged circulation. ACS Appl Bio Mater. 2022;5(2):650–660.
- Crane LM, van Oosten M, Pleijhuis RG, Motekallemi A, Dowdy SC, Cliby WA, et al. Intraoperative imaging in ovarian cancer: fact or fiction? *Mol Imaging*. 2011;10(4): 248–257.
- Kalli KR, Oberg AL, Keeney GL, Christianson TJ, Low PS, Knutson KL, et al. Folate receptor alpha as a tumor target in epithelial ovarian cancer. *Gynecol Oncol.* 2008; 108(3):619–626.
- Ebert B, Riefke B, Sukowski U, Licha K. Cyanine dyes as contrast agents for nearinfrared imaging in vivo: acute tolerance, pharmacokinetics, and fluorescence imaging. *J Biomed Opt.* 2011;16(6), 066003.
- Vankayala R, Mac JT, Burns JM, Dunn E, Carroll S, Bahena EM, et al. Biodistribution and toxicological evaluation of micron- and nano-sized erythrocyte-derived optical particles in healthy swiss webster mice. *Biomater Sci.* 2019;7(5):2123–2133.
- 34. Deng Z, Lin J, Bud'ko SL, Webster B, Kalin TV, Kalinichenko VV, et al. Dual targeting with cell surface electrical charge and folic acid via superparamagnetic fe(3)o(4) @cu(2-x)s for photothermal cancer cell killing. Cancers (Basel). 2021;13(21):5275.
- Mac JT, Vankayala R, Lee CH, Anvari B. Erythrocyte-derived nanoparticles with folate functionalization for near infrared pulsed laser-mediated photo-chemotherapy of tumors. Int J Mol Sci. 2022;23(18):10295.
- Tang JC, Partono A, Anvari B. Near-infrared-fluorescent erythrocyte-mimicking particles: physical and optical characteristics. *IEEE Trans Biomed Eng.* 2019;66(4): 1034–1044.
- Zhang YN, Poon W, Tavares AJ, McGilvray ID, Chan WCW. Nanoparticle-liver interactions: cellular uptake and hepatobiliary elimination. *J Control Release*. 2016; 240:332–348.
- Joshi N, Walter JM, Misharin AV. Alveolar macrophages. Cell Immunol. 2018;330: 86–90.
- Kashiwagi S, Choi HS. Ovarian cancer-targeted near-infrared fluorophores for fluorescence-guided surgery. Ann Transl Med. 2023;11(6):274.
- Tanyi JL, Randall LM, Chambers SK, Butler KA, Winer IS, Langstraat CL, et al. A phase iii study of pafolacianine injection (otl38) for intraoperative imaging of folate receptor-positive ovarian cancer (study 006). *J Clin Oncol*. 2023;41(2): 276–284.
- Mahalingam SM, Kularatne SA, Myers CH, Gagare P, Norshi M, Liu X, et al. Evaluation of novel tumor-targeted near-infrared probe for fluorescence-guided surgery of cancer. J Med Chem. 2018;61(21):9637–9646.
- **42.** Hoogstins CE, Tummers QR, Gaarenstroom KN, de Kroon CD, Trimbos JB, Bosse T, et al. A novel tumor-specific agent for intraoperative near-infrared fluorescence imaging: a translational study in healthy volunteers and patients with ovarian cancer. *Clin Cancer Res.* 2016:22(12):2929–2938.
- 43. Vergote I, Bergfeldt K, Franquet A, Lisyanskaya AS, Bjermo H, Heldring N, et al. A randomized phase iii trial in patients with recurrent platinum sensitive ovarian cancer comparing efficacy and safety of paclitaxel micellar and cremophor elpaclitaxel. Gynecol Oncol. 2020;156(2):293–300.
- Boere I, Vergote I, Hanssen R, Jalving M, Gennigens C, Ottevanger P, et al. Cinova: a phase ii study of cpc634 (nanoparticulate docetaxel) in patients with platinum resistant recurrent ovarian cancer. Int J Gynecol Cancer. 2023;33(8):1247–1252.
- Krasner CN, Campos SM, Young CL, Chadda KR, Lee H, Birrer MJ, et al. Sequential phase ii clinical trials evaluating crlx101 as monotherapy and in combination with bevacizumab in recurrent ovarian cancer. *Gynecol Oncol.* 2021;162(3):661–666.
- 46. Gabizon AA, Patil Y, La-Beck NM. New insights and evolving role of pegylated liposomal doxorubicin in cancer therapy. In: Drug Resistance Updates: Reviews and Commentaries in Antimicrobial and Anticancer Chemotherapy. 29. 2016:90–106.
- Ma WW, Tolcher AW, Perez CA, Orr D, Hamilton EP, Zhao Y, et al. Phase 1 trial of a novel c'dot drug conjugate (cdc), elu001, in patients with solid tumors known to overexpress folate receptor alpha (fro.). J Clin Oncol. 2023;41(16\_suppl). TPS3159-TPS
- Patankar NA, Waterhouse D, Strutt D, Anantha M, Bally MB. Topophore c: a liposomal nanoparticle formulation of topotecan for treatment of ovarian cancer. IND. 2013;31(1):46–58.
- Wang L, Li S, Zhu D, Qin Y, Wang X, Hong Z, et al. Effectiveness and safety of nabpaclitaxel and platinum as first-line chemotherapy for ovarian cancer: a retrospective study. J Gynecol Oncol. 2023;34(4), e44.
- Guo T, Yu W, Lv S, Zhang C, Tian Y. Mir-302a inhibits the tumorigenicity of ovarian cancer cells by suppression of sdc1. Int J ClinExp Pathol. 2015;8(5):4869–4880.
- 51. Sun C, Huang Y, Jiang C, Li Z. Updates on fluorescent probes and open-field imaging methods for fluorescence-guided cytoreductive surgery for epithelial ovarian cancer: a review. BJOG: Int J Obstet Gynaecol. 2022;129(suppl 2):50–59.
- Park Y, Li Y, Choi M, Kim J, Lee D. Novel sn-38 double core-shell micelle formulation, snb-101, enhanced anti-tumor effect and tolerance. *Ann Oncol.* 2019; 30:iv20.